Pure and Applied Geophysics

CrossMark

Imaging Rainfall Infiltration Processes with the Time-Lapse Electrical Resistivity Imaging Method

Gang Zhang,[1,2] Gui-Bin Zhang,[1] Chien-chih Chen,[2] Ping-Yu Chang,[2] Tzu-Pin Wang,[2] Horng-Yuan Yen,[2] Jia-Jyun Dong,[3] Chuen-Fa Ni,[3] Su-Chin Chen,[4] Chao-Wei Chen,[5] and Zheng-yuan Jia[1]

Abstract—Electrical Resistivity Imaging (ERI) was carried out continuously for 10 days to map the subsurface resistivity distribution along a potentially hazardous hillslope at the Jieshou Junior High School in Taoyuan, Taiwan. The reliability of the inverted resistivity structures down to about 25 m depth was examined with synthetic modeling using the same electrode arrangements installed on land surface as in field surveys, together with a DOI (depth-of-investigation) index calculated from the ERI data. The subsurface resistivity distribution is consistent with results from well logging. These ERI recordings were taken daily and provided highly resolved imagery of the resistivity distribution underground and illustrated the dynamical fluid-flow behavior due to heavy rainfall infiltration. Using Archie's law, the resistivity distribution was transformed into a map of relative water saturation (RWS), which is strongly correlated with the rainfall infiltration process. We then found that the averaged RWS is significantly correlated with daily precipitation. Our observations indicate that time-lapse ERI is effective in monitoring subterraneous rainfall infiltration; moreover, the preferential flow paths can be delineated according to the changes in averaged RWS derived from the ERI data.

Key words: Electrical resistivity imaging, depth-of-investigation, Archie's law, rainfall infiltration, preferential path.

[1] School of Geophysics and Information Technology, China University of Geosciences, Beijing 100083, China. E-mail: gz.geophysics@outlook.com; gbzhang@cugb.edu.cn; jzy@cugb.edu.cn

[2] Department of Earth Sciences and Graduate Institute of Geophysics, National Central University, Jhongli, Taoyuan 32001, Taiwan. E-mail: chencc@earth.ncu.edu.tw; pingyuc@gmail.com; wtbin@uch.edu.tw; yenhy@earth.ncu.edu.tw

[3] Graduate Institute of Applied Geology, National Central University, Jhongli, Taoyuan 32001, Taiwan. E-mail: jjdong@geo.ncu.edu.tw; nichuenfa@geo.ncu.edu.tw

[4] Department of Soil and Water Conservation, National Chung Hsing University, Taichung 402, Taiwan. E-mail: scchen@nchu.edu.tw

[5] Land Engineering Consultants Co., Ltd., Nankang, Taipei 115, Taiwan. E-mail: vick@safe100.com.tw

1. Introduction

Electrical resistivity imaging (ERI) has been widely used in resource exploration, hydrogeology surveys, engineering geology surveys, and environment geology surveys (Ahmed and Sulaiman 2001; Chang et al. 2012; De Bari et al. 2011; Drahor et al. 2011; Fikos et al. 2012; Hermans et al. 2012a, b; Lehmann et al. 2013; Long et al. 2006; Maiti et al. 2012; Martinez-Pagan et al. 2010; Metwaly et al. 2013; Muchingami et al. 2012; Perrone et al. 2014; Pujari et al. 2007; Revil et al. 2010; Singh et al. 2010; Sirhan and Hamidi 2013; Sonkamble 2014; Springman et al. 2013; Tang et al. 2007; Travelletti et al. 2012). It can also be used for monitoring the groundwater flow and river water discharge patterns (Coscia et al. 2011, 2012; Hayley et al. 2009; Suzuki and Higashi 2001). In the recent years, the time-lapse ERI method has been applied to monitor the preferential flow paths within the rock/soil mass (Drahor et al. 2011; Hermans et al. 2012b; Maiti et al. 2012; Muchingami et al. 2012) and the geological system of CO_2 storage for the real-time purpose (Bergmann et al. 2012; Christensen et al. 2006; Picotti et al. 2013). Compared with other geotechnical and hydrological methods used for monitoring rainfall infiltration processes, the time-lapse ERI method can perform live, high-resolution monitoring of changes in the physical properties of a subsurface (Perrone et al. 2014) in terms of the variation of subsurface resistivity distribution. Furthermore, ERI is also cost-effective for surveying large areas, comparing to the stream gauging by hydrographic station which is point measurement by several water source wells. It is different from the ERI method, applied stream

gauging in monitoring groundwater flow by hydrographic station is hard to achieve a highly-resolved imagery of the resistivity distribution subsurface for surveying large areas, although it can absolutely provide high-accuracy information of variations in rainfall infiltration processes for real time.

This study is primarily focused on measuring the variation of subsurface resistivity distribution to frequently monitor the changes in groundwater flow due to heavy rainfall infiltration by ERI method. The very fact of frequently monitoring by ERI method that the low-resistivity zone can be described and tracked in each frequency, therefore, the preferential flow paths can be delineated from the variation of subsurface low-resistivity zone and the dynamical fluid-flow behavior due to heavy rainfall infiltration can be illustrated. Furthermore, by using Archie's Law, a map of relative water saturation (RWS) can be produced from ERI images, in which case the subsurface variations in rainfall infiltration processes are clearly expressed.

Generally, there are lots of research achievements about application of ERI in monitoring groundwater flow due to infiltration of river water (COSCIA et al. 2012) and monitoring the preferential flow paths within the soil mass (MAITI et al. 2012), imaging artificial salt water infiltration (HERMANS et al. 2012b), and so on, however, there are few applications of time-lapse ERI method in monitoring the rainfall infiltration for real time at a potentially hazardous hillslope which is meaningful and valuable. From the time-lapse ERI method, we can get the high-resolution subsurface electrical conductivity distribution for real time; then, the changes of subsurface electrical conductivity grid block and RWS are monitored for the period of the rainfall infiltration. Based on the subsurface resistivity, RWS map obtained from resistivity inversion and the information from the other data such as drilling data and rainfall amount from the weather report, the landslide slippage surface and predominant pathway of rainfall can be evaluated.

2. Forward Solution and Inversion Strategy for ERI

The equation governing the DC (direct current) response due to a point current source is given by (TELFORD et al. 1976; TELFORD and SHERIFF 1990):

$$\nabla \cdot (\sigma \nabla \phi) = -I\delta(\mathbf{r} - \mathbf{r_s}), \qquad (1)$$

where ϕ is the electrical potential [V], I is the source current [A], $\delta(\mathbf{r} - \mathbf{r_s})$ is the delta function, $\mathbf{r}$ and $\mathbf{r_s}$ are the location of the observation point and current-source point [m], respectively, and σ is the electrical conductivity [S/m].

The discretization of the resistivity problem discussed here is based on a theory described by (DEY and MORRISON 1979). Using the finite difference method to the resistivity modeling, the unknown potential at all of the nodes in the grid is evaluated using incomplete Cholesky-conjugate gradient (ICCG) technique to obtain accurate and stable solutions. Since the simulation of the whole space is restricted to the homogeneous half-space, it is required that the boundary conditions be specified at each point. Neumann (no-current) boundary conditions

$$\frac{\partial \phi}{\partial \mathbf{n}} = 0 \qquad (2)$$

are assigned at the ground surface, $z = 0$, whereas Robin boundary conditions

$$\frac{\partial \phi}{\partial \mathbf{n}} + \frac{\phi}{r}\cos\theta = 0 \qquad (3)$$

are assigned far from the source, where θ is the angle between the radial distance r and the outward normal $\mathbf{n}$.

For direct current resistivity inversion, the smoothness-constrained least-squares optimization method (DEGROOT-HEDLIN and CONSTABLE 1990; ELLIS and OLDENBURG 1994; MARESCOT and LOKE 2003; RODI and MACKIE 2001) is frequently used. Here, an iteratively reweighted version of this method

$$\left(\mathbf{J_i^T R_d J_i} + \lambda_i \mathbf{W^T R_m W}\right)\Delta\boldsymbol{\rho_i}$$
$$= \mathbf{J_i^T R_d g_i} - \lambda_i \mathbf{W^T R_m W}\rho_{i-1} \qquad (4)$$

was employed for resistivity inversion, where $\mathbf{g_i}$ is the data misfit vector describing the difference between the observed values and calculated potential or apparent resistivity from the forward solution, $\Delta\boldsymbol{\rho_i}$ is the change in the model parameters for the ith iteration, $\boldsymbol{\rho_{i-1}}$ is the model-parameters vector for the previous iteration, $\mathbf{J}$ is the Jacobian matrix of partial derivatives, $\mathbf{W}$ is the roughness filter, $\mathbf{R_d}$ and $\mathbf{R_m}$ are weighting matrices introduced so that different

elements of the data misfit and model roughness vectors are given equal weights in the inversion process, and λ_i is the damping factor after the ith iteration, calculated by

$$\lambda_i = \lambda_0 / 10^i \qquad (5)$$

with an initially large value ($\lambda_0 = 10^8$ in this paper).

The number of forward problems per inversion iteration is one of most influence factors on the efficiency of inverse problem. In the course of resistivity inversion, comparing two king of methods on computing the Jacobian (sensitivity) matrix which include a directly solving $\mathbf{J}$ (YORKEY *et al.* 1987) and a similar procedure for $\mathbf{J}$ multiplying an arbitrary vector $\mathbf{x}$ (MACKIE and MADDEN 1993; RODI 1976), we prefer employing Rodio's method. Because Yorkey's method is required doing one forward problem for each model parameter for each inversion iteration on one current source, and the amount of calculation is great when the grid mesh density is high, the influence of the mesh grid density to the inverse of efficiency is enormous; however, the approach for computing $\mathbf{Jx}$ and $\mathbf{J^T y}$ (Rodio's method) requires only one forward problem for each inversion iteration on one current source. For the resistivity inversion problem with the multiple current sources, Rodi's method is much more efficient and appropriate for this case in field study.

Based on these principles, rapid 2D inversion algorithms that use conjugate-gradient relaxation techniques to solve the maximum-likelihood inverse equations were developed for ERI data using the C# language.

3. Simulation Modeling for Estimating the Depth of Investigation

Determining a depth of investigation (DOI) is one of th important problems in geophysical inversion. According to the field study, the ERI method with the surface array was used for imaging rainfall infiltration processes. Therefore, a synthetic resistivity model with surface array employed for resistivity modeling and inversion need to be established for synthetic DOI study. What is more, to figure out the sensitivity of ERI data to the conductivity blocks in depth when a surface array is installed in the ERI surveys, a synthetic resistivity model with a stair-shaped

conductive (10 Ω m) inclusion inside a resistive background (100 Ω m) is built according to the inverted resistivity maps of the field study for 8 days (Fig. 5) and mathematical statistics study of the values of inverted resistivity blocks. This model (Fig. 1a) consists of 140 resistivity blocks, and the data space comprises 686 observations of electric potential difference for various dipole–dipole arrangements taken in the field survey.

The inverted model (Fig. 1b) bears considerable likeness to the true resistivity model (Fig. 1a). The background value of the inverted model is nearly 100 Ω m, and the near-surface inhomogeneities consisting of the stair-shaped resistivity distribution is well delineated down to 25 m deep.

For thoroughly testifying the conclusion of the testing, a contrast test adopted the alike method. A synthetic resistivity model with a stair-shaped conductive (10 Ω m) inclusion inside a resistive background (100 Ω m) is built. This model (Fig. 1d) consists of 70 resistivity blocks and 686 observations. The inverted model (Fig. 1e) illustrated that the stair-shaped resistivity distribution is well delineated and the depth penetration of inversion with the surface electrical array is 25 m.

Overall, the DOI of inversion can extend 25 m when we carry out the surface array in filed study. The purpose of numerical simulation and inversion for the synthetic resistivity model with the surface array is to estimate the DOI of inversion in the case of electrode arrangements installed in field study, and the DOI from the simulation modeling is critical for the following inversion of the ERI field data.

4. Estimating the depth of investigation using field data

The simulations based on field arrangements, as discussed in "Simulation Modeling for Estimating the Depth of Investigation", illustrate that the DOI is mainly qualitative (CATERINA *et al.* 2013). However, there are several tools to evaluate the inverted images including the model resolution matrix ($\mathbf{R}$), the cumulative sensitivity matrix ($\mathbf{S}$), and the DOI-index. According to previous research results, (CATERINA *et al.* 2011, 2013; DECEUSTER *et al.* 2014), the numerical
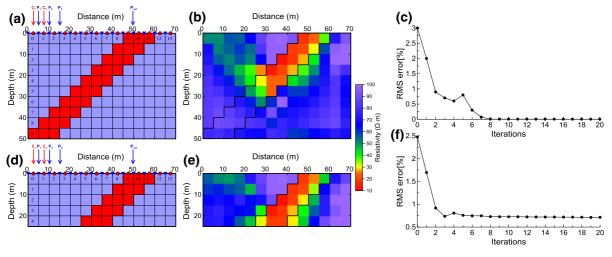
Figure 1

The simulated resistivity model with a *stair-shaped* conductive inclusion inside a resistive *background* and *inverted* image. **a** True resistivity model, which is used to generate synthetic data where the forward modeling grid has 14×10 *rectangular* nodes, and is 70 m wide and 50 m deep. The electrode arrangement is a dipole–dipole array with the current and potential electrodes placed on the surface. The resistivities of the elements are 100 Ω m (*blue cells*) and 10 Ω m (*red cells*). **b** Inverted resistivity model. The number of iterations is 20, and the initial value for the damping factor (λ_0) is 10^8. **c** The root mean square (*RMS error*) of the inversion is 0.14 % at 20th iteration. **d**–**f** The second synthetic resistivity model, inverted resistivity model, and RMS *error* which is employed for comparison testing. The forward modeling grid has 14×5 *rectangular* nodes, and is 70 m wide and 25 m deep with the same electrode array and same number of the ERI data for inversion

benchmark shows that indicators based on **R** and **S** are the most appropriate to appraise resistivity maps in terms of the exactitude of inverted parameters, and the DOI index providing mainly qualitative information for the reliability of inverted images. The DOI index is more appropriate for this case study on depth of prospecting of inversion with the electrode arrangements installed on land surface, and different electrode array geometries have different depths of penetration (OLDENBURG and LI 1999). DOI index is very important for estimating the reliability of inverse modeling because it indicates where the inverted image is well constrained by the data and where it is not. The calculation of DOI index needs to be implemented stringently. The empirical DOI index method provides more accurate information from ERI data measured in field. This method was introduced by (OLDENBURG and LI 1999) and modified by (MARESCOT *et al.* 2003).

In general, this method involves two inversions carried out using reference models with different initial resistivity values. The resistivity of the first reference model is obtained from the averaging the apparent resistivity. The second reference model is usually set at ten times that of the first one (LOKE

2001). From the modeled resistivity values, the following DOI index is calculated:

$$R_{1,2}(x,z) = \frac{m_1(x,z) - m_2(x,z)}{m_{1r} - m_{2r}}, \qquad (6)$$

where m_{1r} and m_{2r} are the resistivity of the first and second reference models, respectively, and $m_1(x,z)$ and $m_2(x,z)$ are the respective model-cell resistivities obtained from the first and second inversions. The distribution in the region of DOI indices trends to zero, where the inversion produces the same cell resistivity regardless of the reference-model resistivity. The cell resistivity with zero DOI index is, therefore, well-constrained by the data and initial resistivity model implemented for inversion has negligible impact on inverse modeling. However, in the region where there is poorly constrained cell-resistivity data, $R(x,z)$ will trend to unity due to the fact that inverted resistivity is similar to the initial resistivity. Thus, the model resistivity in regions where $R(x,z)$ is small are considered "reliable", while in areas of high $R(x,z)$ are not. To reduce the effect of the damping factor and the choice of the two initial reference models, the DOI index can be normalized
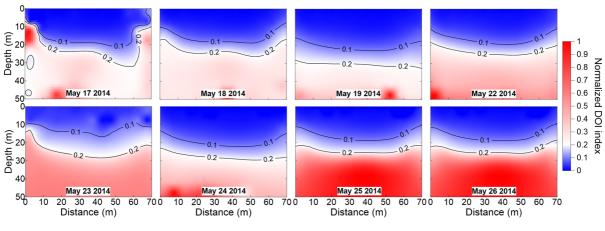
Figure 2
Normalized DOI-index cross-section for 8 days (from 17 May to 26 May, 2014) and the DOI indices of 0.1 and 0.2 are denoted with *black solid lines*

with the maximum value R_{max} of $R(x,z)$ from Eq. (6) as follows (MARESCOT *et al.* 2003; ROBERT *et al.* 2011)

$$R(x,z) = \frac{m_1(x,z) - m_2(x,z)}{R_{max}(m_{1r} - m_{2r})} \qquad (7)$$

The model for calculating the DOI index uses cells that extend to the edges of the survey line, and its depth range is roughly three to five times the median DOI for the largest array spacing used (LOKE 2001).

Figure 2 shows a 50-m-deep DOI cross-section for the ERI data. Figure 2a, b represents two inverse modeling from resistivity inversion using different reference models with different resistivity value. The first reference model is obtained from the average of the apparent resistivity values, $\sim 100\ \Omega$ m. Figure 2c shows the normalized DOI index, calculated after a second inversion using an initial model with ten times the resistivity of the first initial model, $\sim 1000\ \Omega$ m.
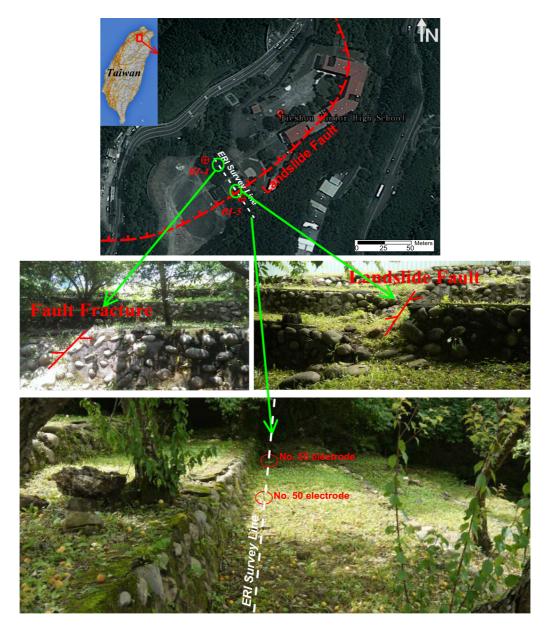
The normalized DOI-index region (Fig. 2c) shows that the model resistivity, in areas of 20-meter depth or greater, is reliable when the DOI index is 0.1. Meanwhile, the model resistivity is reliable at depths of 25 m or more when the DOI index is 0.2.

According to the synthetic resistivity modeling with a stair-shaped conductive inclusion inside a resistive background, the DOI can reach to about 25 m when the length of the survey line is 70 m. Incorporating the DOI-index cross-section, we can set the DOI to 25 m for the inversion of our ERI field data collected at Jieshou Junior High School.

5. Results

ERI surveys were conducted continuously at Jieshou Junior High School in Northwestern Taiwan for 10 days from May 17th to May 26th 2014, though the data on the 20th and 21st were corrupted due to lightning strikes. The ERI survey line is perpendicular to the landslide scarp line as shown in Fig. 3. The mass body shown was creeping to the northwest continuously and a sliding scarp was found across the Jieshou Junior High School. In order to monitor rainfall infiltration processes in the subsoil, and delineate the preferential flow paths and flow velocities, our dipole–dipole ERI surveys included 686 observations of electric potential difference, taken daily, with a survey-line length of 70 m and potential-electrode spacing of 5 m (Fig. 4a). According to simulated synthetic resistivity modeling and the DOI-index region calculated from the ERI for May 17th, the most reasonable depth of inversion was taken as 25 m. Then, the ERI-data inversion was performed.

The ERI inversions show that the ERI method can produce high-resolution images (Figs. 4b, 5) of the subterranean resistivity distribution. Some surface objects are reflected in the ERI images (Fig. 4b), such as fault fracture and flowerbeds, which are marked in the first ERI image. Furthermore, the subsurface resistivity distribution obtained from inversion of field ERI data is consistent with results from well logging (Fig. 4b). The thickness of the high-

Figure 3
Aerial map of Jieshou Junior High School, Taoyuan, Taiwan. The ERI survey *line* is *perpendicular* to the landslide fault strike. There are two *boreholes* for monitoring the water level. Two regions of fault fracture and two potential electrodes installed in land surface are marked

resistivity layer reaches to 5 m that corresponds to the backfilling bed according to drilling data of two boreholes. The low-resistivity layer below the backfilling bed corresponds to the tuffaceous clastic rock. Meanwhile, according to the weather report, there was heavy rain sometime after May 19th (see the hyetograph of 10 days in Fig. 7), the changes in electrical characteristics between the maps of May 19th and 22nd are obvious (Fig. 5). It can be inferred that the low-resistivity zone extended mostly along the landslide slippage surface (which marked in Fig. 5) from May 22nd to the 24th; what is more, there is compresso-crushed zone on the land surface (see Fig. 3) corresponding to the projection position of the subsurface landslide slippage surface (between the distance of 30 m and 40 m along the survey line).
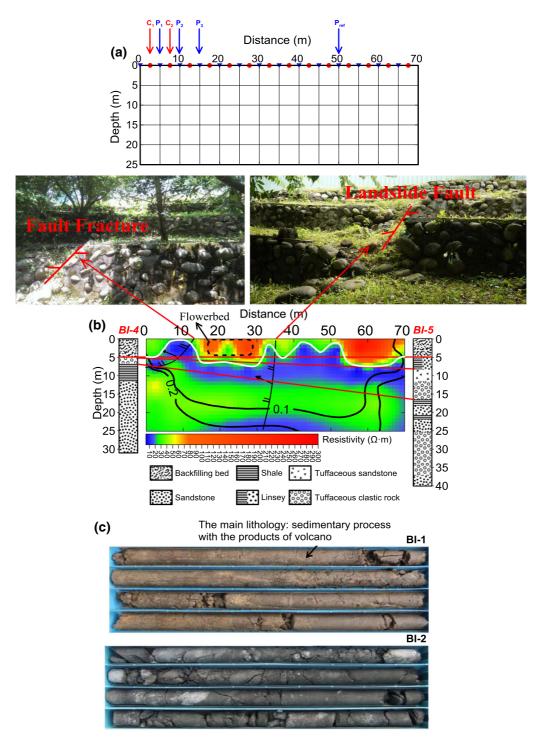
Figure 4
Inversion of ERI data measured at Jieshou Junior High School. **a** Electrode arrangements used for field survey and *grid mesh* implemented for inversion. **b** Shown are two DOI-index curves (at 0.1 and 0.2) are marked by *solid black lines* and drilling data of two boreholes. In the image, some characteristics of the surface have been marked, including a fault fracture and a flowerbed. **c** The core samples from the other two local boreholes (BI-1 and BI-2) and the depth of BI-1 and BI-2 wells is 30 and 70 m, respectively
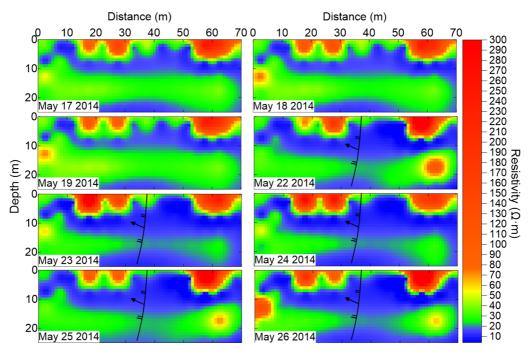
Figure 5
Inversion of ERI data measured at Jieshou Junior High School for 8 days. The *black solid line* marked in the resistivity maps from May 22 to 26 representS the slip plane

In addition, the inverted resistivity can be transformed to RWS using Archie's Law (ARCHIE 2013), as shown in the following Eq. (8):

$$\rho = a\phi^{-m}S_w^{-n}\rho_w, \qquad (8)$$

where ρ is the bulk resistivity of the rock, ρ_w is the resistivity of the pore water, and for short period of monitoring time, the resistivity of the pore water can be approximated to be constant value, ϕ is the volume fraction porosity, S_w is the fractional water saturation, a is the proportionality constant, m is the cementation factor, and n is the saturation exponent.

The original RWS is derivable from the Archie's Law, as shown in the following Eq. (9). $RWS^{k,t1}$ is the water saturation of the *t2*th day relative to the *t1*th day for the *k*th grid block. $S_w^{k,t1}$, $\phi_{k,t1}^{-m}$, $\rho_w^{k,t1}$, $\rho^{k,t1}$, $a^{k,t1}$, $m^{k,t1}$ and $n^{k,t1}$ stand for the fractional water saturation, volume fraction porosity, resistivity of the pore water, bulk resistivity of the rock, proportionality constant, cementation factor, and saturation exponent of the *k*th grid block on the *t1*th day, respectively.

$$
\begin{aligned}
RWS^{k,t1} &= \frac{\Delta S_w^{k,t1}}{S_w^{k,t1}} = \frac{S_w^{k,t2} - S_w^{k,t1}}{S_w^{t1}} \\
&= \frac{\left(a^{k,t2}\phi_{k,t2}^{-m^{k,t2}}\rho_w^{k,t2} \big/ \rho^{k,t2}\right)^{\frac{1}{n^{k,t2}}} - \left(a^{k,t1}\phi_{k,t1}^{-m^{k,t1}}\rho_w^{k,t1} \big/ \rho^{k,t1}\right)^{\frac{1}{n^{k,t1}}}}{\left(a^{k,t1}\phi_{k,t1}^{-m^{k,t1}}\rho_w^{k,t1} \big/ \rho^{k,t1}\right)^{\frac{1}{n^{k,t1}}}} \\
&= \frac{\left(a^{k,t2}\phi_{k,t2}^{-m^{k,t2}}\rho_w^{k,t2} \big/ \rho^{k,t2}\right)^{\frac{1}{n^{k,t2}}}}{\left(a^{k,t1}\phi_{k,t1}^{-m^{k,t1}}\rho_w^{k,t1} \big/ \rho^{k,t1}\right)^{\frac{1}{n^{k,t1}}}} - 1
\end{aligned}
$$
$$(9)$$

Because ERI was carried out continuously for only 10 days, it can be considered that there is little change in volume fraction porosity, resistivity of the pore water, proportionality constant, and cementation factor in a short period of time. So the properties of the *k*th element can be stated as follows:

$$a^{k,t2} = a^{k,t1},$$
$$m^{k,t2} = m^{k,t1},$$
$$\phi_{k,t2}^{-m^{k,t2}} = \phi_{k,t1}^{-m^{k,t1}},$$
$$\rho_w^{k,t2} = \rho_w^{k,t1}.$$

then, the Eq. (9) can be written

$$RWS^{k,t1} = \left(\frac{\rho^{k,t2}}{\rho^{k,t1}}\right)^{-\frac{1}{n}} - 1 \qquad (10)$$

The substituting resistivity maps into RWS by the Eq. (10). The resulting RWS map provides a more intuitive reflection of the variation of subsurface rainfall infiltration and a more accurate estimation of subterraneous rainfall infiltration processes and flow velocities, comparing with the ones from the inverted resistivity images.

However, when the resistivity of the pore water is sufficiently high that the electric conductivity of the mineral grains is a substantial contribution to the electric conductivity of the aquifer, the formulations of Archie are no longer valid (KIRSCH 2006). Modified formulations are also required for material with surface conductivity like clay.

The calculation of the resistivity of clayey material is presented by (FROHLICH and PARKE 1989). They assume that the bulk conductivity of clayey material σ can be explained by parallel connection of surface conductivity $\sigma_{Surface}$ and conductivity of pore water σ_W with volumetric water content Θ,

$$\sigma = \frac{1}{a} \cdot \sigma_W \cdot \Theta^k + \sigma_{Surface} \qquad (11)$$

With the Archie's Law and the expression of surface conductivity by (RHOADES et al. 1989a, b), we can get the RWS of the clay layer as described by Eq. (12) based on similar principles;

$$RWS^{k,t1} = \left(\frac{\sigma^{k,t2} - \sigma_{Surfer}}{\sigma^{k,t1} - \sigma_{Surfe}}\right)^{\frac{1}{n}} - 1 \qquad (12)$$

or, expressed in terms of resistivity

$$RWS^{k,t1} = \left(\frac{1/\rho^{k,t2} - \sigma_{Surfer}}{1/\rho^{k,t1} - \sigma_{Surfe}}\right)^{\frac{1}{n}} - 1 \qquad (13)$$

For the surveyed area, the clay content of the backfilling bed is low with a small surface area. Moreover, the depth of 5 m below in the surveyed area is consolidated formation (see Fig. 4c). According to the results from the core analysis data of the local two boreholes, the main lithology in the surveyed area is the sedimentary process with the products of a volcano. Therefore, the influence of clay content in near-surface can be neglected.

Equation (10), illustrates that uncertainties exist in the saturation exponent n and the saturation exponent has the effect in the value of RWS; however, it will not affect in the variation tendency of RWS during the 8 days. Moreover, we care about the variation tendency of RWS for the 8 days but not the value of RWS in each day. Therefore, the value of RWS needs only to be calculated with $n = 2.0$ by the Eq. (10).

The RWS maps (Fig. 6) show a significant correlation with rainfall infiltration. Figure 5 shows there was little rainfall on May 18th and 19th, and heavy rainfall after the 19th. The shallow water has infiltrated on the 23rd and 24th, because the value of RWS reduced significantly compared to the 22nd. However, the RWS increased on the 25th for the near-surface (up to 5 m, shown in red) because of heavy rainfall on that day. On the 26th, the near-surface becomes blue because of rapid infiltration of rainwater. This indicates that the probability of landslides is very low since the agglomerate rainfall on the landslide slippage surface was infiltrated quickly and without sustained hydraulic pressure throughout the landslide slippage surface.

The daily precipitation is significantly correlated with the averaged change of the RWS each day, as shown in Fig. 7. Here, two values of average RWS are calculated from the RWS images within the $R = 0.1$ and $R = 0.2$ contour intervals, depending on different DOI indices. The curves show that the daily hyetograph is very similar to the two curves of the averaged RWS. Therefore, the rainfall is significantly correlated with the average RWS, which validates our use of Archie's law to produce RWS images from ERI data to evaluate rainfall infiltration.

Furthermore, Fig. 8 shows variations of the average RWS at different depths between the 10- to 20-m and the 30- to 40-m distance marks on the survey line. It is implemented for further delineating preferential flow paths and slip plane, because there are two fracture zones between the 10- to 20-m and the 30- to 40-m distance at land surface (Fig. 4b). Most of the RWS variation curves in Fig. 8a show only a slight deviation during the observation period, except for the one indicating a 2.5-m depth. On the other hand, the variation curves in Fig. 8b indicate a downward migration of the RWS peak plume. These findings suggest that the wetting front moved through
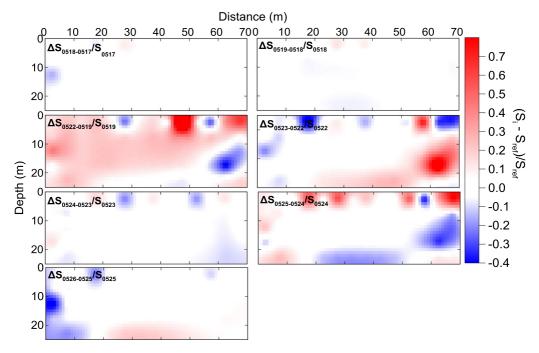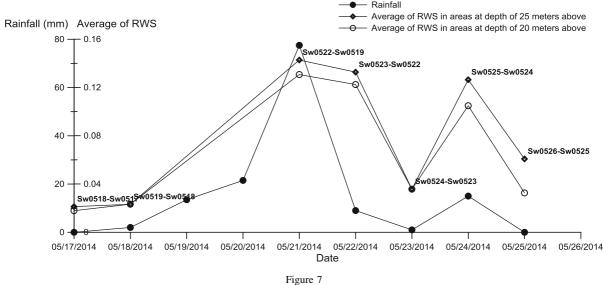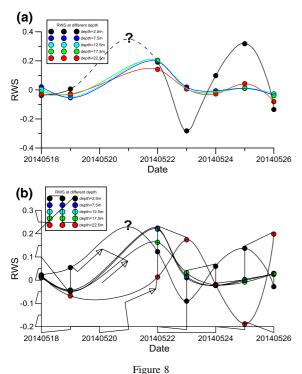
Figure 6
Relative water saturation (RWS) map with the saturation exponents $n = 2.0$. $\Delta S_{0518-0517}/S_{0517}$ stands for the water saturation of May 18th relative to May 17th

Figure 7
Hyetograph and average RWS for depths of up to 20 and 25 m, with the DOI index at 0.1 and 0.2, respectively

a preferential path occurring between the 10- and 20-m mark on the survey line. Thus, the infiltration took place very rapidly and we are not able to find a gradually moving wetting plume here. Furthermore, we are able to estimate the infiltration rate between 30 and 40 m from the migration of the RWS peak induced by the rain. An infiltration rate of 4 m/day can be calculated from the slope of the migrating

Figure 8
Variations of the average RWS at depths between **a** 10- to 20-m and **b** 30- to 40-m distance marks on the survey *line*

RWS-variation peaks in the region. We assert that this infiltration rate applies to undisturbed soil and may be much higher through the preferential path existing between 10 and 20 m.

6. Discussion and Conclusions

ERI was carried out on a hillslope using a dipole–dipole array with the current and potential electrodes installed on the land surface, making a valid DOI necessary for inversion interpreting. There are some appraisal tools regularly used in inverted images, such as the model resolution matrix, the cumulative sensitivity matrix, and the DOI-index. However, the DOI-index can be used for evaluating the reliability of inverse modeling, and it is appropriate for the inversion of field ERI data with electrode arrangements installed on land surface. The two methods used to evaluate the DOI for inversion were in agreement: the first simulated resistivity model with a stair-shaped conductive inclusion inside a resistive background and predicted a DOI close to about 23 m:

the second method, namely DOI-index sectioning, indicated that the modeled resistivity was reliable for a depth of 25 m along a 70-m-long survey line. Then, based on these previews, an initial resistivity model with 70 m in distance and 25 m in depth is employed for inversions of acquired ERI data for 8 days were performed.

The inversions confirm the viability of ERI in tracking the movement of groundwater flow and rainfall infiltration by recording the variation of subsurface resistivity distribution. Meanwhile, RWS maps can be obtained from ERI images via Archie's Law, which provide a more intuitive reflection of the variation of subsurface rainfall infiltration, preferential flow paths, and slip plane. The average RWS, meanwhile, is calculated from RWS images at depths of up to 20 and 25 m in our case. After careful study and comparison, a hyetograph was produced that was very similar to the two curves of average RWS. From the hyetograph, the rainfall is significantly correlated with the average RWS; thus the rainfall infiltration characteristics evaluated by RWS images is reliable.

Overall, time-lapse ERI method is for the first time applied to monitor the rainfall infiltration for real time at a potentially hazardous hillslope. It is meaningful and valuable for us to provide much more information about variation of subsurface resistivity distribution. According to the changes of subsurface electrical resistivity distribution, we can better understand the landslide hazard combining with hydrologic data from the stream gauging. Comparing to the stream gauging by hydrographic station which is point measurement by several water source wells, ERI can obtain the highly resolved imagery of the resistivity distribution underground. Joint inversion or investigation of the ERI data from field survey and hydrologic data from stream gauging in a potentially hazardous hillslope should be a development trend of technique for prediction and evaluation of landslide in the future.

REFERENCES

A.M. AHMED and W.N. SULAIMAN 2001. *Evaluation of groundwater and soil pollution in a landfill area using electrical resistivity imaging survey*. Environmental Management 28, 655–663.

G.E. ARCHIE 2013. *The Electrical Resistivity Log as an Aid in Determining Some Reservoir Characteristics*. Transactions of the AIME 146, 54–62. doi:10.2118/942054-g

P. BERGMANN, C. SCHMIDT-HATTENBERGER, D. KIESSLING, C. RUCKER, T. LABITZKEL, J. HENNINGES, G. BAUMANN and H. SCHUTT 2012. *Surface-downhole electrical resistivity tomography applied to monitoring of CO2 storage at Ketzin, Germany*. Geophysics 77, B253–B267. doi:10.1190/Geo2011-0515.1

D. CATERINA, J. BEAUJEAN, T. ROBERT and F. NGUYEN 2011. *Image appraisal tools for electrical resistivity tomography. In: Image appraisal tools for electrical resistivity tomography.*

D. CATERINA, J. BEAUJEAN, T. ROBERT and F. NGUYEN 2013. *A comparison study of different image appraisal tools for electrical resistivity tomography*. Near Surface Geophysics 11, 639–657. doi:10.3997/1873-0604.2013022

P.Y. CHANG, C.C. CHEN, S.K. CHANG, T.B. WANG, C.Y. WANG and S.K. HSU 2012. *An investigation into the debris flow induced by Typhoon Morakot in the Siaolin Area, Southern Taiwan, using the electrical resistivity imaging method*. Geophysical Journal International 188, 1012–1024. doi:10.1111/j.1365-246X.2011.05310.x

N.B. CHRISTENSEN, D. SHERLOCK and K. DODDS 2006. *Monitoring CO2 injection with cross-hole electrical resistivity tomography*. Exploration Geophysics 37, 44–49. doi:10.1071/Eg06044

I. COSCIA, S.A. GREENHALGH, N. LINDE, J. DOETSCH, L. MARESCOT, T. GUNTHER, T. VOGT and A.G. GREEN 2011. *3D crosshole ERT for aquifer characterization and monitoring of infiltrating river water*. Geophysics 76, G49–G59. doi:10.1190/1.3553003

I. COSCIA, N. LINDE, S. GREENHALGH, T. VOGT and A. GREEN 2012. *Estimating traveltimes and groundwater flow patterns using 3D time-lapse crosshole ERT imaging of electrical resistivity fluctuations induced by infiltrating river water*. Geophysics 77, E239–E250. doi:10.1190/Geo2011-0328.1

C. DE BARI, V. LAPENNA, A. PERRONE, C. PUGLISI and F. SDAO 2011. *Digital photogrammetric analysis and electrical resistivity tomography for investigating the Picerno landslide (Basilicata region, southern Italy)*. Geomorphology 133, 34–46. doi:10.1016/j.geomorph.2011.06.013

J. DECEUSTER, A. ETIENNE, T. ROBERT, F. NGUYEN and O. KAUFMANN 2014. *A modified DOI-based method to statistically estimate the depth of investigation of dc resistivity surveys*. Journal of Applied Geophysics 103, 172–185. doi:10.1016/j.jappgeo.2014.01.018

C. DEGROOT-HEDLIN and S. CONSTABLE 1990. *Occam's inversion to generate smooth, two-dimensional models from magnetotelluric data*. Geophysics 55, 1613–1624.

A. DEY and H.F. MORRISON 1979. *Resistivity modeling for arbitrarily shaped three-dimensional structures*. Geophysics 44, 753–780. doi:10.1190/1.1440975

M.G. DRAHOR, M.A. BERGE, G. GOKTURKLER and T.O. KURTULMUS 2011. *Mapping aquifer geometry using electrical resistivity tomography: a case study from Sanliurfa, south-eastern Turkey*. Near Surface Geophysics 9, 55–66. doi:10.3997/1873-0604.2010052

R.G. ELLIS and D.W. OLDENBURG 1994. *Applied Geophysical Inversion*. Geophysical Journal International 116, 5–11. doi:10.1111/j.1365-246X.1994.tb02122.x

I. FIKOS, G. VARGEMEZIS, J. ZLOTNICKI, J.R. PUERTOLLANO, P.B. ALANIS, R.C. PIGTAIN, E.U. VILLACORTE, G.A. MALIPOT and Y. SASAI 2012. *Electrical resistivity tomography study of Taal volcano hydrothermal system, Philippines*. Bulletin of Volcanology 74, 1821–1831. doi:10.1007/s00445-012-0638-5

R.K. FROHLICH and C.D. PARKE 1989. *The electrical resistivity of the vadose zone—field survey*. Groundwater 27, 524–530.

K. HAYLEY, L.R. BENTLEY and M. GHARIBI 2009. *Time-lapse electrical resistivity monitoring of salt-affected soil and groundwater*. Water Resources Research 45. doi:10.1029/2008wr007616

T. HERMANS, A. VANDENBOHEDE, L. LEBBE, R. MARTIN, A. KEMNA, J. BEAUJEAN and F. NGUYEN 2012. *Imaging artificial salt water infiltration using electrical resistivity tomography constrained by geostatistical data*. Journal of Hydrology 438-439, 168–180. doi:10.1016/j.jhydrol.2012.03.021

T. HERMANS, A. VANDENBOHEDE, L. LEBBE and F. NGUYEN 2012. *A shallow geothermal experiment in a sandy aquifer monitored using electric resistivity tomography*. Geophysics 77, B11–B21. doi:10.1190/Geo2011-0199.1

R. KIRSCH 2006. *Groundwater geophysics*. Springer.

P. LEHMANN, F. GAMBAZZI, B. SUSKI, L. BARON, A. ASKARINEJAD, S.M. SPRINGMAN, K. HOLLIGER and D. OR 2013. *Evolution of soil wetting patterns preceding a hydrologically induced landslide inferred from electrical resistivity survey and point measurements of volumetric water content and pore water pressure*. Water Resources Research 49, 7992–8004. doi:10.1002/2013wr014560

M.H. LOKE 2001. Tutorial: 2-D and 3-D electrical imaging surveys.

H. LONG, H. MIZUNAGA and K. USHIJIMA 2006. *Borehole-to-surface electrical data interpretation at Takigami geothermal field in Kyushu, Japan using neural network. In: Borehole-to-surface electrical data interpretation at Takigami geothermal field in Kyushu, Japan using neural network*, pp. 1318–1322. Society of Exploration Geophysicists.

R.L. MACKIE and T.R. MADDEN 1993. *Three-dimensional magnetotelluric inversion using conjugate gradients*. Geophysical Journal International 115, 215–229.

S. MAITI, V.C. ERRAM, G. GUPTA and R.K. TIWARI 2012. *ANN based inversion of DC resistivity data for groundwater exploration in hard rock terrain of western Maharashtra (India)*. Journal of Hydrology 464-465, 294–308. doi:10.1016/j.jhydrol.2012.07.020

L. MARESCOT and M.H. LOKE 2003. *Using the Depth of Investigation Index Method in 2D Resistivity Imaging for Civil Engineering Surveys. In: Using the Depth of Investigation Index Method in 2D Resistivity Imaging for Civil Engineering Surveys*, pp. 540–547.

L. MARESCOT, M.H. LOKE, D. CHAPELLIER, R. DELALOYE, C. LAMBIEL and E. REYNARD 2003. *Assessing reliability of 2D resistivity imaging in mountain permafrost studies using the depth of investigation index method*. Near Surface Geophysics 1, 57–67.

P. MARTINEZ-PAGAN, A.F. CANO, G.R.R. DA SILVA and A.B. OLIVARES 2010. *2-D Electrical Resistivity Imaging to Assess Slurry Pond Subsoil Pollution in the Southeastern Region of Murcia,*

Spain. Journal of Environmental and Engineering Geophysics *15*, 29–47.

M. METWALY, M.A. KHALIL, E. AL-SAYED and A. EL-KENAWY 2013. *Tracing subsurface oil pollution leakage using 2D electrical resistivity tomography*. Arabian Journal of Geosciences *6*, 3527–3533. doi:10.1007/s12517-012-0600-z

I. MUCHINGAMI, D.J. HLATYWAYO, J.M. NEL and C. CHUMA 2012. *Electrical resistivity survey for groundwater investigations and shallow subsurface evaluation of the basaltic-greenstone formation of the urban Bulawayo aquifer*. Physics and Chemistry of the Earth *50*-52, 44–51. doi:10.1016/j.pce.2012.08.014

D.W. OLDENBURG and Y.G. LI 1999. *Estimating depth of investigation in dc resistivity and IP surveys*. Geophysics *64*, 403–416. doi:10.1190/1.1444545

A. PERRONE, V. LAPENNA and S. PISCITELLI 2014. *Electrical resistivity tomography technique for landslide investigation: A review*. Earth-Science Reviews *135*, 65–82. doi:10.1016/j.earscirev.2014.04.002

S. PICOTTI, D. GEI, J.M. CARCIONE, V. GRÜNHUT and A. OSELLA 2013. *Sensitivity analysis from single-well ERT simulations to image CO2 migrations along wellbores*. The Leading Edge *32*, 504–512. doi:10.1190/tle32050504.1

P.R. PUJARI, P. PARDHI, P. MUDULI, P. HARKARE and M.V. NANOTI 2007. *Assessment of pollution near landfill site in Nagpur, India by resistivity imaging and GPR*. Environmental Monitoring and Assessment *131*, 489–500. doi:10.1007/s10661-006-9494-0

A. REVIL, T.C. JOHNSON and A. FINIZOLA 2010. *Three-dimensional resistivity tomography of Vulcan's forge, Vulcano Island, southern Italy*. Geophysical Research Letters *37*, 1–5. doi:10.1029/2010gl043983

J.D. RHOADES, N.A. MANTEGHI, P.J. SHOUSE and W.J. ALVES 1989. *Estimating Soil-Salinity from Saturated Soil-Paste Electrical-Conductivity*. Soil Science Society of America Journal *53*, 428–433.

J.D. RHOADES, N.A. MANTEGHI, P.J. SHOUSE and W.J. ALVES 1989. *Soil Electrical-Conductivity and Soil-Salinity - New Formulations and Calibrations*. Soil Science Society of America Journal *53*, 433–439.

T. ROBERT, A. DASSARGUES, S. BROUYERE, O. KAUFMANN, V. HALLET and F. NGUYEN 2011. *Assessing the contribution of electrical resistivity tomography (ERT) and self-potential (SP) methods for a water well drilling program in fractured/karstified limestones*. Journal of Applied Geophysics *75*, 42–53. doi:10.1016/j.jappgeo.2011.06.008

W.L. RODI 1976. *A technique for improving the accuracy of finite element solutions for magnetotelluric data*. Geophysical Journal International *44*, 483–506.

W. RODI and R.L. MACKIE 2001. *Nonlinear conjugate gradients algorithm for 2-D magnetotelluric inversion*. Geophysics *66*, 174–187. doi:10.1190/1.1444893

U.K. SINGH, R.K. TIWARI and S.B. SINGH 2010. *Inversion of 2-D DC resistivity data using rapid optimization and minimal complexity neural network*. Nonlinear Processes in Geophysics *17*, 65–76.

A. SIRHAN and M. HAMIDI 2013. *Detection of soil and groundwater domestic pollution by the electrical resistivity method in the West Bank, Palestine*. Near Surface Geophysics *11*, 371–380. doi:10.3997/1873-0604.2013012

S. SONKAMBLE 2014. *Electrical resistivity and hydrochemical indicators distinguishing chemical characteristics of subsurface pollution at Cuddalore coast, Tamil Nadu*. Journal of the Geological Society of India *83*, 535–548. doi:10.1007/s12594-014-0081-7

S.M. SPRINGMAN, A. THIELEN, P. KIENZLER and S. FRIEDEL 2013. *A long-term field study for the investigation of rainfall-induced landslides*. Geotechnique *63*, 1177–1193. doi:10.1680/geot.11.P.142

K. SUZUKI and S. HIGASHI 2001. *Groundwater flow after heavy rain in landslide-slope area from 2-D inversion of resistivity monitoring data*. Geophysics *66*, 733–743. doi:10.1190/1.1444963

J.T. TANG, J.F. ZHANG, B. FENG, J.Y. LIN and C.S. LIU 2007. *Determination of borders for resistive oil and gas reservoirs by deviation rate using the hole-to-surface resistivity method*. Chinese Journal of Geophysics-Chinese Edition *50*, 926–931.

W.M. TELFORD and R.E. SHERIFF 1990. *Applied geophysics*. Cambridge university press.

W. TELFORD, L. GELDART, R. SHERIFF and D. KEYS 1976. *Applied Geophysics Ch 5. In: Applied Geophysics Ch 5*. Cambridge University Press, New York.

J. TRAVELLETTI, P. SAILHAC, J.P. MALET, G. GRANDJEAN and J. PONTON 2012. *Hydrological response of weathered clay-shale slopes: water infiltration monitoring with time-lapse electrical resistivity tomography*. Hydrological Processes *26*, 2106–2119. doi:10.1002/hyp.7983

T.J. YORKEY, J.G. WEBSTER and W.J. TOMPKINS 1987. *Comparing reconstruction algorithms for electrical impedance tomography*. IEEE Trans Biomed Eng *34*, 843–852.